Therefore, with this mixed likelihood, we have a slight decrease of the intrinsic and the total dispersions.

Lusso & Risaliti (2017) proposed a toy model for the $L_X - L_{UV}$ relation, where the relation arises from the dependence of both quantities on the black hole mass $M_{BH}$ and the black hole accretion rate $\dot{M}_{BH}$. Said model predicts the slope between the X-ray luminosity (or flux) and the FWHM of the Mg II line to be $\hat{\eta} = 0.44^{+0.21}_{-0.19}$, and they found, for a sample of 545 quasars, an observed slope between the X-ray luminosity and the Mg II FWHM equal to $\eta_{LR17} = 0.54 \pm 0.07$, consistent with the toy model. Our result, $\eta = 0.25 \pm 0.04$, is also consistent with the prediction of the toy model. It significantly differs from the Lusso & Risaliti (2017) value, but we note that they performed the analysis (i) for the sample as a whole and not in redshift bins, using ΛCDM-derived luminosities, and (ii) using the photometric 2500 Å luminosity as $L_{UV}$ instead of the spectroscopic one. If we perform the analysis in the same way, using the photometric luminosities for our sample, we obtain $\eta_{phot} = 0.45 \pm 0.04$, which is statistically consistent with the Lusso & Risaliti (2017) result.

However, our results do not entirely align with the toy model presented Lusso & Risaliti (2017). The model, indeed, implied also the presence of a $L_{UV}$–FWHM relation, while we find the two quantities to be uncorrelated. At the same time, it might be that the small dynamic range of the Mg II FWHM does not allow us to observe the correlation.

Since the observational dependence of the X-ray flux on the Mg II FWHM line may be due to a physical dependence on the black hole mass, we performed an additional check by repeating our whole analysis for two subsamples with black hole mass estimates $M_{BH} < 10^{8.9}\,M_\odot$ and $M_{BH} < 10^{8.9}\,M_\odot$, respectively. We did not find any significant differences between these two subsamples. This suggests that the parameters of the relation do not directly depend on the black hole mass.

We finally have to consider that all the results that we have discussed in this subsection might be dependent on the cosmological model used to compute luminosities from fluxes. To test this possible dependence, we followed a cosmographic approach to fit the quasar Hubble diagram, as described in Bargiacchi et al. (2021). We found analogous results in terms of covariance matrices, eigenvectors and $L_{UV}$−FWHM dependence.

## 5. Discussion

The main results obtained through the various fits presented in the previous sections are the following.

First of all, the slope $\gamma$ and the intrinsic dispersion $\delta$ of the X-ray-to-UV relation obtained by using spectroscopically derived 2500 Å fluxes are $\gamma \sim 0.46$ and $\delta \sim 0.22$ dex, respectively.

Among the different proxies of the disc emission that we tested, the monochromatic flux at 2500 Å can be considered as the best available one, given its observational coverage over a broad redshift range. For the X-ray emission in the X-ray-to-UV relation, we find instead that the best monochromatic indicator (i.e., the one providing the smallest intrinsic dispersion) is the 1-keV flux.

When adopting the Mg II line flux as UV proxy, the obtained intrinsic dispersion is smaller than that obtained with monochromatic continuum fluxes ($\delta_{Mg\,II} \sim 0.17$ dex). The slope of the relation is instead significantly steeper ($\gamma_{Mg\,II} \sim 0.60$) than in the spectroscopic case. We also find that when the 'photometric estimate' of the UV monochromatic flux is adopted, the best-fit parameters (both slope and dispersion) are consistent with those found using the Mg II line flux as UV proxy.

Finally, when the logarithm of the FWHM of the Mg II line is added to the relation, a statistically significant correlation is found, with a negligible decrease of the total intrinsic dispersion. The Mg II FWHM and UV flux parameters are not statistically correlated.

Here we discuss the interpretation and the main consequences of these results. The most remarkable result of our analysis is arguably that the spectroscopically derived 2500 Å monochromatic flux delivered a significantly lower $\gamma$ value when used as $f_{UV}$ compared to the Mg II line flux. This trend can be explained as a consequence of the non-linear relation between the emission-line equivalent width (EW) and the luminosity of the quasar continuum, known as the Baldwin effect (Baldwin 1977). We analysed the relation between the Mg II luminosity and the monochromatic luminosity at 2500 Å derived from the spectroscopic analysis of our sample and we obtained a slope of ∼0.8. In order to fit the whole sample simultaneously, for this analysis we used luminosities instead of fluxes, assuming a standard flat ΛCDM model with $\Omega_M = 0.3$ and $H_0 = 70\,\mathrm{km\,s^{-1}\,Mpc^{-1}}$. We checked that the results are not significantly dependent on the choice of the cosmological model.

If we now consider the relation between the X-ray and UV luminosities as $\log(L_{2\,keV}) = \gamma \log(L_{2500}) + \beta$, with $\gamma = 0.46$ as shown in Sect. 2, and we use the $\log(L_{2500}) - \log(L_{Mg\,II})$ mentioned above, we obtain a slope of the $\log(L_{2\,keV}) - \log(L_{Mg\,II})$ of $0.46/0.8 = 0.58$, which is fully consistent with the slope of the relation that we obtain when using the Mg II luminosity (or flux) as $L_{UV}$, as shown in Sect. 4. Therefore, we conclude that the reason behind different X-ray to UV relations when shifting from continuum UV proxies to line proxies is associated with the presence of the Baldwin effect itself.

Another result related to the adoption of the Mg II as UV proxy is the smaller intrinsic dispersion $\delta$ of the X-ray to UV relation with respect to the monochromatic continuum indicators. Considering that this line requires an ionising continuum at wavelengths shorter than 824 Å, a possible interpretation of this result is that an even tighter relation must exist between the X-ray flux and the UV flux blueward of the Ly limit. In this scenario, the monochromatic fluxes at optical or near-UV wavelengths are all 'secondary indicators' with a similar relation to the primary one.

The slope parameter that we obtain when using the 'photometric' UV flux has a less obvious interpretation. The photometric flux is a complex UV proxy, as it contains contributions from both the quasar continuum and line emissions. Moreover, even if it is formally a monochromatic quantity, it is derived from the wide-band photometric fluxes. We notice that its value is similar to the one obtained using the Mg II line as a UV proxy and that the dispersion of the relation is marginally better than the one obtained with truly monochromatic fluxes. This suggests that the combined information used to derive the photometric flux is similar to that contained in the Mg II flux, and is more closely related to the UV emission at $\lambda \sim 800$ Å than the monochromatic fluxes.

In Fig. 7, we show the relation between the luminosity of the Mg II line and the photometric luminosity at 2500 Å. The slope is statistically consistent with unity, which explains the similar behaviour of these two quantities when used as $f_{UV}$ proxies in the X-ray-to-UV relation.

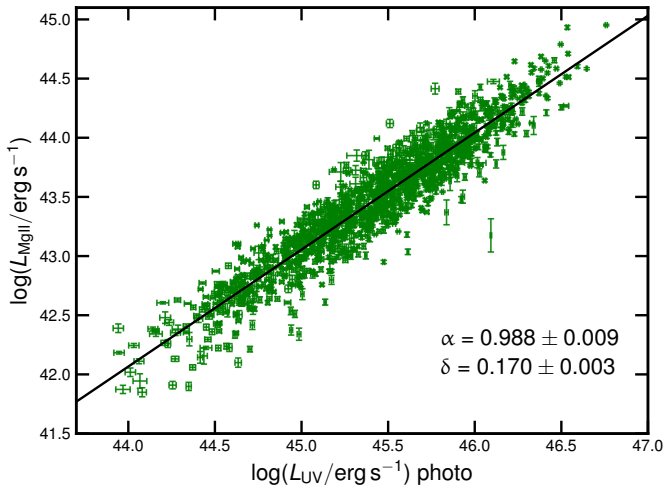


**Fig. 7.** Relation between the luminosity of the Mg II line and the luminosity at 2500 Å derived from photometry.

## 6. Cosmological application

The most relevant result of our analysis concerning the use of quasars as standard candles through the X-ray-to-UV relation is the confirmation of such relation with spectroscopic data. Since there are no known standard candles at redshifts higher than ∼1.5, it is impossible to have an 'external' test of the validity of the relation in a cosmology-independent way. The only way to confirm or falsify the method is through an analysis of the possible redshift dependent physical and/or selection effects that may bias the distance estimate. In this sense, the complete UV (rest-frame) spectral analysis is a significant step forward; possible biases related to the use of the optical broad-band magnitudes (e.g., due to dust reddening or to the effect of strong lines moving into or out of the photometric bands depending on the redshift) are ruled out, and the flux measurements are directly done from the spectral fits.

The second fundamental outcome of our work is the first systematic search of the best X-ray and UV proxies of the relation, within the spectral range covered by the available spectroscopic data. While the best X-ray and UV indicators turned out to be the monochromatic flux at 1 keV and the Mg II flux, respectively, we found that the intrinsic dispersion of the relation with the other proxies is only slightly larger. In particular, the 'standard' indicators, which are the monochromatic flux at 2500 Å derived from the photometric data and the monochromatic flux at 2 keV, are almost as effective as the 'best' ones.

This result suggests that none of the indicators used here is the primary driver of the relation. In order to prove this statement, we can consider our best UV indicator, that is the Mg II flux and the intrinsic dispersion of the X-ray–UV relation, $\delta_{\rm Mg\,II}$, obtained with this indicator. If the Mg II flux were the primary driver of the relation (i.e., the physical relation involves either the Mg II flux or a tightly related quantity), we would expect that the dispersion $\delta$ of the X-ray-to-UV relation using another UV proxy would be related to $\delta_{\rm Mg\,II}$ through the following relation: $\delta^2 = \delta^2_{\rm Mg\,II} + \Delta^2$, where $\Delta$ is the dispersion of the relation between the Mg II flux and the other UV indicator. However, this is not the case; for example, the dispersion of the relation between the Mg II flux and the monochromatic flux at 2500 Å is $\Delta = 0.15$ dex, which would imply $\delta \sim 0.25$ dex, while the observed value is $\delta = 0.19 \pm 0.01$ dex (see Fig. 6). We conclude that both the UV indicators used here are proxies of a more fundamental one, probably related to the UV emission blueward of the Lyman limit.

A final result with some implications for the use of quasars as standard candles is the relation between the X-ray and UV fluxes and the FWHM of the Mg II emission line. We tested the inclusion of this parameter in the X-ray-to-UV flux relation, using the photometric 2500 Å flux as $f_{\rm UV}$. Just like in the spectroscopic case, we found that there is no correlation between the UV flux and the Mg II FWHM. Therefore, we can incorporate an additional term in the relation between fluxes when the FWHM of the Mg II emission line is available, while fitting the 'traditional' relation if not. When doing so, we obtain $\gamma = 0.58 \pm 0.01$, $\delta = 0.16$ dex, and $\delta_{\rm T} = 0.19$ dex.

We applied the results discussed above to the construction of a new Hubble diagram of quasars, based on the spectroscopic quasar sample described in this work. We derived the luminosity distances using Eq. (9) for objects for which the Mg II line is available, and the standard relation for those for which it is not. We used the 1-keV monochromatic flux as $f_{\rm X}$. As for $f_{\rm UV}$, we used both the spectroscopic and the photometric monochromatic flux at 2500 Å (we also repeated the computation using the Mg II flux, obtaining fully consistent results). The results are shown in Fig. 8, where we also plot the supernovae of the Pantheon sample (Scolnic et al. 2018), used for the absolute calibration. Petrosian et al. (2022) argued that the analysis in redshift intervals may bias the cosmological analysis. We stress that we never considered any binning (especially when considering redshifts) to perform the cosmological analysis in our previous works. The same consideration can be applied here as well. The distance modulus of each individual quasar is obtained from Eqs. (9) and (10), and the fits of the Hubble diagram are done by marginalising over the parameters $\gamma$ and $\beta$ of the relation. As a consequence, the red points shown in Fig. 8 are computed only after the best fit values of these parameters are obtained, and they are shown only for illustrative purposes.

The Hubble diagram in Fig. 8 is relevant for two main reasons. First, the two versions of the diagram, with the two different methods to derive the UV monochromatic flux, are in full agreement. This was not granted a priori; if some systematic effect related to the derivation of the photometric fluxes were present, it would have been revealed by the comparison with the spectroscopy-based values. The photometric fluxes are much easier to obtain, and indeed we always used these values in our previous works. Therefore, this result is also a validation of the Hubble diagrams in Risaliti & Lusso (2019) and Lusso et al. (2020), which revealed a strong tension with the 'concordance' flat ΛCDM model.

Second, the dispersion in the Hubble diagram based on spectroscopic points is significantly lower than that based on photometric fluxes. This is the consequence of the different slopes of the X-ray-to-UV relation depending on which UV flux is used: $\gamma_{\rm phot} \sim 0.6$ for the photometric fluxes and $\gamma_{\rm spec} \sim 0.45$ for the spectroscopic ones. Considering the error propagation from the relation to the distance moduli plotted in Fig. 8, the main contribution to the error is the intrinsic dispersion of the relation, divided by a factor $(1 - \gamma)$. This term implies that the uncertainty on the distances derived from spectroscopic fluxes is lower that of distances based on photometric fluxes by a factor of $(1 - \gamma_{\rm phot})/(1 - \gamma_{\rm spec}) \sim 0.75$.

The tension with the standard flat ΛCDM model of the spectroscopic sample discussed in this paper has a statistical significance of $3\sigma$. This is lower than previously published results based on larger samples (Lusso et al. 2020; Bargiacchi et al. 2021)

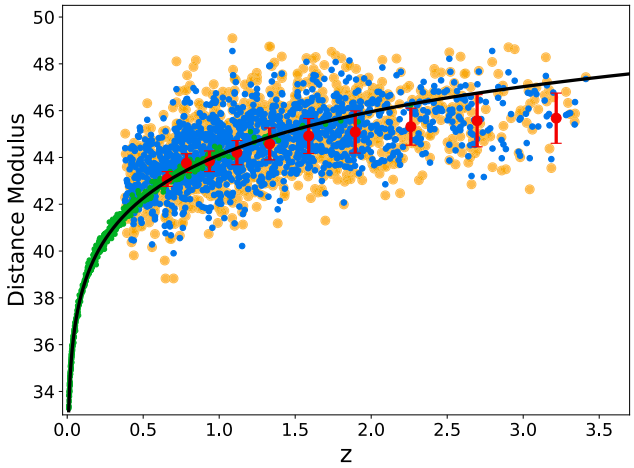


**Fig. 8.** Hubble diagram of supernovae and quasars. Green points are supernovae Ia from the Pantheon sample (Scolnic et al. 2018), yellow points are quasars with distances derived using the photometric UV fluxes, blue points are quasars with distances derived using the spectroscopic UV fluxes, and red points are the average distance modulus values for spectroscopic quasars in the individual redshift bins. The normalisation parameter for quasars is chosen in order to match that of supernovae Ia. As in our previous studies (Risaliti & Lusso 2019), we do so by cross-matching the Hubble diagram of quasars with that of supernovae in the common redshift range. The black line represents the prediction of a flat ΛCDM model with $\Omega_M = 0.3$.

but, again, it is the first result based on a sample with complete control on the derivation of the UV fluxes.

## 7. Summary and conclusions

In this paper, we present a thorough UV spectral analysis of 1764 quasars from the Lusso et al. (2020) sample with the main aims being to discuss the choice of the $L_X$ and $L_{UV}$ indicators and to establish whether it is possible to further reduce the observed dispersion to gain a better understanding of the physics behind the $L_X$–$L_{UV}$ relation. We thus derived monochromatic luminosities at five different wavelengths as well as the emission-line properties. We compared our results with the spectral analysis of Wu & Shen (2022) and we found a good agreement (see Appendix A). We also computed the X-ray properties of our sample from a spectroscopic analysis for objects at a redshift higher than 1.9, while we used photometric data for objects at lower redshift (see Appendix B). Our main results are summarised below.

1. We obtained the monochromatic flux at 2500 Å from a detailed spectroscopic analysis, as this is supposed to be a more accurate measurement than the one derived from the photometric data. We then analysed the $L_X$–$L_{UV}$ relation in narrow redshift bins so that we could (i) use fluxes instead of luminosities and therefore be independent of any chosen cosmology, and (ii) look for possible redshift trends of the slope parameter $\gamma$. While the slope is confirmed not to show any systematic trend with redshift, its value of $\gamma \sim 0.46$ is lower (flatter) than those found in our previous studies where photometric data were used. Also, the dispersion parameter $\delta$ is slightly higher when using spectroscopically derived monochromatic fluxes as $f_{UV}$. If the true physical quantity behind the $L_X$–$L_{UV}$ relation had been the monochromatic luminosity at 2500 Å (or any of the wavelengths that we tested; see below) we would have expected better results in terms of the dispersion. As this does not occur, it probably means that the spectroscopic and the photometric luminosities are simply two different proxies of another quantity, and thus they are similarly effective when used in the X-ray-to-UV relation.
2. We investigated what the best energies to be used as $L_X$ and $L_{UV}$ are, following the assumption that both the UV and the X-ray continua of quasars can be parameterised as power laws and studying the dependence of the X-ray-to-UV relation on the respective spectral slopes. We stress that we do not expect the relation to subsist between two monochromatic luminosities, but we are looking for the best possible proxies for the overall UV (disc) and X-ray (corona) emission. In the X-rays, we find that there is a preference for 1 keV as the characteristic energy, as it is the one less sensitive to the actual spectral slope. When using the 1-keV fluxes instead of the 2-keV ones, we indeed found a lower dispersion. Unfortunately, given the redshift range of our sample, the 1-keV flux is on average measured with higher uncertainties than the 2-keV ones. This partly undermines the advantage of having found the characteristic energy because the resulting total dispersion is only slightly lower. Still, the fact that the total dispersion decreases even if we are using a 'worse' proxy in terms of uncertainties means that physically the relation is indeed tighter when we are using the 1-keV flux as $f_X$. In the UV, we find no conclusive indications on a specific characteristic wavelength. This might be explained if the 'true' physical quantity is found at much shorter wavelengths, beyond the peak of the disc emission, so assuming the optical–UV power law is less appropriate and/or informative. Consequently, we argue that the best choice is the 2500 Å flux simply because it is the one that results in a marginally lower dispersion. This might be because this wavelength falls in the observed spectra for the wider redshift range in our sample, implying a lower number of objects for which fluxes are determined via extrapolation and therefore with larger uncertainties.
3. When using the integrated Mg II line flux as $f_{UV}$, we obtain a higher (steeper) slope value ($\gamma \sim 0.6$) and a lower dispersion ($\delta = 0.16$ dex) compared to any other UV continuum indicator derived from the spectroscopic analysis. We note that although the Mg II emission line is found at 2800 Å, its flux strongly depends on the quasar emission at much shorter wavelengths, around ~800 Å. Therefore, it might be that the physical relation behind the X-ray and UV luminosities is more strongly linked to the quasar emission at shorter wavelengths, and that as a consequence the Mg II emission-line flux works as a better proxy when compared to the fluxes in the 1350–5500 Å range. Unfortunately, the Mg II emission line is only available for the objects in our sample up to $z \sim 2.5$. Another possible explanation is that when we consider an indicator such as the Mg II emission line, which strongly depends on the extreme-UV SED shape, a tighter correlation with the soft X-ray can naturally arise due to the energy proximity of the bands involved.
4. The comparison between the values of the slopes that we found when using, respectively, the Mg II line fluxes and the spectroscopic monochromatic fluxes, is entirely consistent with the presence of the Baldwin effect.
5. We confirm a correlation between the X-ray and UV flux taking into account the FWHM of the Mg II line, while the UV flux and the FWHM turn out to be not significantly

correlated. This non-correlation allows us to include the FWHM in the X-day/UV flux relation whenever available, and to keep using the standard relation otherwise. In this way, we can overcome the redshift limitations on the Mg II flux and still obtain a lower dispersion for the whole sample.

6. The Hubble diagram obtained from spectroscopic UV data is fully consistent with that obtained with photometric data. This is a validation of the previous results based on 'photometric' Hubble diagrams. Moreover, the 'spectroscopic' Hubble diagram shows a tension at statistical level of $\sim 3\sigma$ with the flat ΛCDM model. In previous works (e.g., Lusso et al. 2020; Bargiacchi et al. 2021), we obtained a higher significance of this tension, thanks to a wider redshift extent than the sample considered here. However, the Hubble diagram presented here is the first one where we have fully checked the UV spectral properties of the sources (and also the X-ray ones at $z > 1.9$).

Overall, the results presented in this work are another step towards the validation of the non-linear X-ray-to-UV relation of quasars as a reliable distance indicator. Since a limited of number of supernovae Ia are available at redshifts higher than ∼1.5 and, by construction, a cosmology-independent validation of the method is impossible, the only way to further check our method is to search for possible evolutionary effects in the spectral emission of the quasars included in our Hubble diagram. In Sacchi et al. (2022), we demonstrated that the average continuum and line properties of quasars at $z > 2.5$ are perfectly matched to the ones of lower redshift counterparts in both the UV and X-rays. An extensive analysis of the stacked SDSS spectra in bins of BH mass and Eddington ratio for all the sources of the current sample is currently ongoing (Trefoloni et al., in prep.). We expect that future observations of supernovae at $z > 1.5$ will be able to independently probe any deviation from the concordance model found with the Hubble diagram of quasars.

*Acknowledgements.* We thank the referee for their detailed and constructive suggestions. We acknowledge financial contribution from the agreement ASI-INAF n.2017-14-H.O. EL acknowledges the support of grant ID: 45780 Fondazione Cassa di Risparmio Firenze.

## References

Arnaud, K. A. 1996, in Astronomical Data Analysis Software and Systems V, eds. G. H. Jacoby, & J. Barnes, ASP Conf. Ser., 101, 17
Baldwin, J. A. 1977, ApJ, 214, 679
Bargiacchi, G., Risaliti, G., Benetti, M., et al. 2021, A&A, 649, A65
Bargiacchi, G., Benetti, M., Capozziello, S., et al. 2022, MNRAS, 515, 1795
Calderone, G., Nicastro, L., Ghisellini, G., et al. 2017, MNRAS, 472, 4051
Elvis, M., Hao, H., Civano, F., et al. 2012, ApJ, 759, 6
Foreman-Mackey, D., Hogg, D. W., Lang, D., & Goodman, J. 2013, PASP, 125, 306
Haardt, F., & Maraschi, L. 1991, ApJ, 380, L51
Haardt, F., & Maraschi, L. 1993, ApJ, 413, 507
Khadka, N., & Ratra, B. 2021, MNRAS, 502, 6140
Krolik, J. H., & Kallman, T. R. 1988, ApJ, 324, 714
Lusso, E., & Risaliti, G. 2016, ApJ, 819, 154
Lusso, E., & Risaliti, G. 2017, A&A, 602, A79
Lusso, E., Comastri, A., Vignali, C., et al. 2010, A&A, 512, A34
Lusso, E., Risaliti, G., Nardini, E., et al. 2020, A&A, 642, A150
Lusso, E., Nardini, E., Bisogni, S., et al. 2021, A&A, 653, A158
Meyer, F., Liu, B. F., & Meyer-Hofmeister, E. 2000, A&A, 361, 175
Netzer, H. 1980, ApJ, 236, 406
Petrosian, V., Singal, J., & Mutchnick, S. 2022, ApJ, 935, L19
Rakshit, S., Stalin, C. S., & Kotilainen, J. 2020, ApJS, 249, 17
Richards, G. T., Lacy, M., Storrie-Lombardi, L. J., et al. 2006, ApJS, 166, 470
Risaliti, G., & Lusso, E. 2019, Nat. Astron., 3, 272
Sacchi, A., Risaliti, G., Signorini, M., et al. 2022, A&A, 663, L7
Sanders, D. B., Phinney, E. S., Neugebauer, G., Soifer, B. T., & Matthews, K. 1989, ApJ, 347, 29
Scolnic, D. M., Jones, D. O., Rest, A., et al. 2018, ApJ, 859, 101
Scolnic, D., Brout, D., Carr, A., et al. 2022, ApJ, 938, 113
Shakura, N. I., & Sunyaev, R. A. 1973, A&A, 24, 337
Steffen, A. T., Strateva, I., Brandt, W. N., et al. 2006, AJ, 131, 2826
Svensson, R. 1982, ApJ, 258, 321
Svensson, R., & Zdziarski, A. A. 1994, ApJ, 436, 599
Tananbaum, H., Avni, Y., Branduardi, G., et al. 1979, ApJ, 234, L9
Wu, Q., & Shen, Y. 2022, ApJS, 263, 82
Young, M., Elvis, M., & Risaliti, G. 2010, ApJ, 708, 1388

## Appendix A: UV spectral analysis

We performed the fit of the SDSS UV spectra for the 1764 objects in our sample with the IDL package `QSFit` Calderone et al. (2017). This software allowed us to fit the AGN continuum, the Balmer continuum, the emission-line and iron-complex properties, and the host-galaxy component. Regarding the host galaxy, a single template of an elliptical galaxy was used to determine its contribution to the total luminosity. The code is highly customizable, and our main settings are as follows: for quasars with redshifts below 0.6, given that the host-galaxy luminosity can be a relevant share of the total luminosity, the slope of the quasar continuum is degenerate with the host galaxy normalisation. Therefore, there is no way to determine it in a reliable way. We consequently fixed the value of the continuum slope for such quasars as $f_\lambda \propto \lambda^{-1.7}$. Each emission line was fitted with a Gaussian profile. `QSFit` allowed us to consider both a broad and narrow component to fit each line and to add unknown components if necessary. In case the code is not able to correctly disentangle the broad and the narrow component of the main emission lines, we used a composite profile of a broad component and an unknown one to account for the residuals. With this method, what we obtained are the *total* emission line properties, rather than the separated properties of broad and narrow components. Full width at half maximum (FWHM) upper limits were set to 2000 km/s for unknown and narrow lines and to 10,000 km/s for broad lines. To avoid fitting regions of the spectrum contaminated by intergalactic absorption, the minimum wavelength for model fitting was set to 1450 Å (rest frame) for all the objects in our sample.

The strength of the `QSFit` code is that the spectral properties are all fitted simultaneously. This way, one can reasonably assume that the obtained continuum properties do not depend on local features of the spectrum itself.

At the end of the fitting procedure, for each quasar we obtained the continuum slope and the monochromatic luminosity at 2500 Å. We also recorded the luminosity values at 1350 Å, 3000 Å, 4400 Å, 5100 Å. If one or more of these wavelengths was out of the spectral range for a given spectrum, we extrapolated its value adopting the best-fit continuum slope. In terms of line properties, we obtained total flux, FWHM, offset velocity, and equivalent width. Together with the line properties and their errors, quality flags for each line were given. Regarding the quality flag, the `QSFit` code automatically raises a flag whenever one or more of the following situations occur: (i) the value of the continuum luminosity, a line's FWHM, or its offset velocity is NaN or equal to zero; (ii) any of the previous quantities hits a boundary value in the fit; (iii) the relative uncertainty on the continuum luminosity is higher than 1.5; (iv) the relative uncertainty on the FWHM of a given line is higher than 2; (v) the uncertainty on the velocity offset is higher than 500 km s$^{-1}$. Objects with bad-quality flags were removed from the sample.

After the fitting procedure, each spectrum was visually inspected and a second quality flag was raised if (i) the residuals of the fitting procedure showed a systematic trend as a function of wavelength or (ii) the mean reduced $\chi^2$ value was higher than 2. Since in these cases the monochromatic luminosities estimates could not be considered reliable, such sources were removed from the sample. As a consequence, our sample size decreased from 1764 to 1705 sources. Among them, 1217 also have good Mg II emission line properties (line luminosity, FWHM, EW, velocity offset), while 403 have H$\beta$, 305 have [O III] $\lambda$4959Å, 291 have [O III] $\lambda$5007Å (202 have both the doublet components), 493 have C IV. In Figure A.1 we show, as an example, the spectra of four objects at different redshifts and the best-fit results of the `QSFit` analysis.

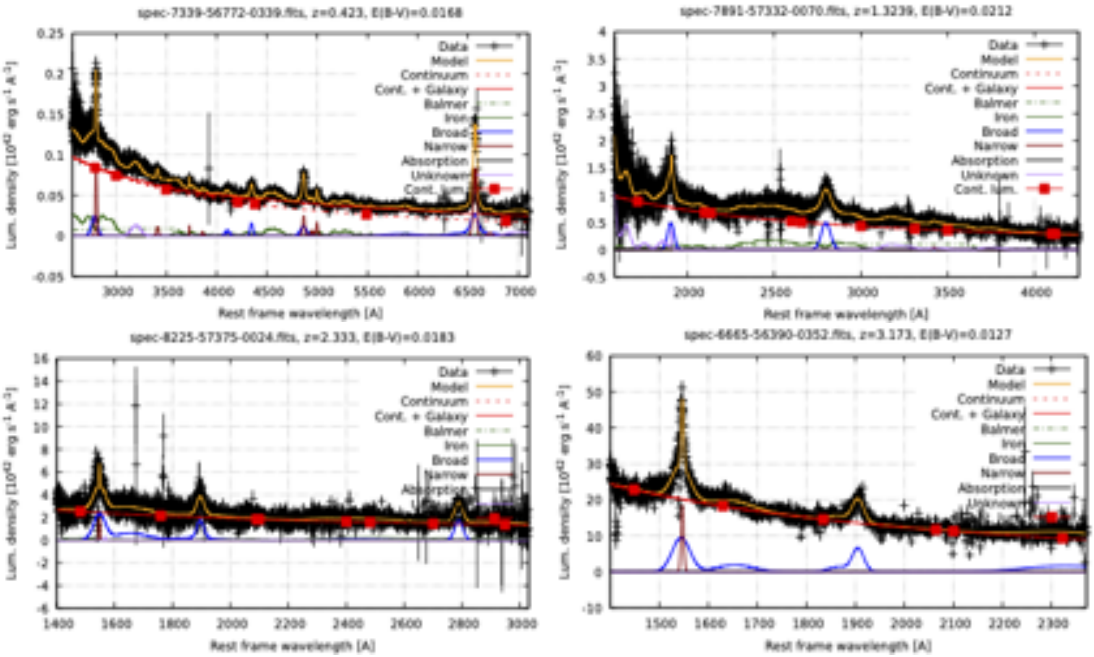


**Fig. A.1.** Four spectra at different redshifts and `QSFit` best-fit results, in yellow. The different components are shown in the legend on the right of each panel.

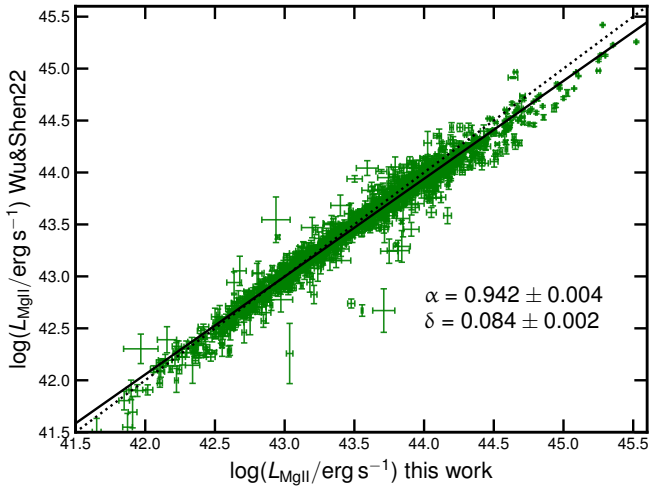


**Fig. A.2.** Comparison between the Mg II luminosity as derived from Wu & Shen (2022) and the Mg II luminosity derived in this work, in logarithmic units (erg s$^{-1}$). The dotted line is the one-to-one relation. We also report the best-fit slope and dispersion and the resulting best-fit-regression line as the solid black line.

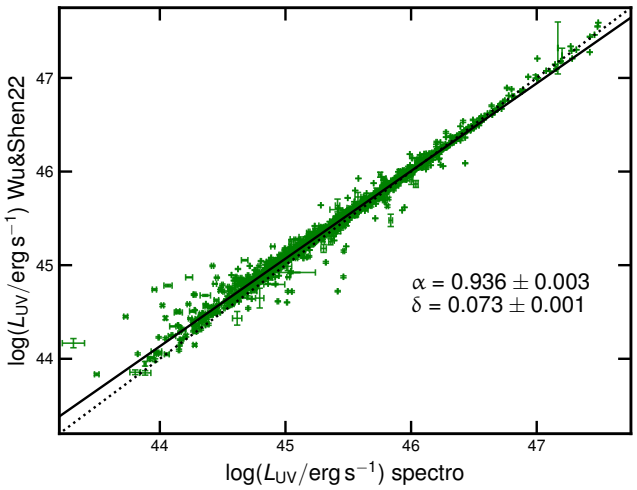


**Fig. A.3.** Comparison between monochromatic luminosity at 2500 Å obtained from our spectral analysis and the one from the Wu & Shen (2022), in logarithmic units (erg s$^{-1}$). The dotted line is the one-to-one relation. We also report the best-fit slope and dispersion and the resulting best-fit regression line with the solid black line. There is an overall good agreement between the two measurements.

In Figure A.2, we compare our estimates of the total luminosity of the Mg II line with the one derived from the Wu & Shen (2022) catalogue. We can see an overall good agreement. Comparisons between other emission line properties show similar results. We also performed the same comparisons with the results of Rakshit et al. (2020), and they gave analogous results.

Wu & Shen (2022) presented the detailed measurements of the spectral properties of ~500,000 quasars from the latest release of the Sloan Digital Sky Survey (SDSS-DR16) quasar catalogue, which were used to validate the results of our spectral analysis. Regarding the monochromatic luminosities, we find a very good match, as can be seen in Figure A.3 for the monochromatic luminosity at 3000 Å. We can also see that the match is excellent at high luminosities, while some scatter is present for less luminous objects. This mainly depends on the different host-galaxy fitting techniques that have been employed; we used a single host-galaxy template, while in Wu & Shen (2022) the galaxy is not characterised. Quasars with lower luminosities are also the ones more affected by the host-galaxy contribution, so we expect higher discrepancies for such objects. Comparisons with the other monochromatic luminosities at different wavelengths (1350 Å, 4400 Å, 5100 Å) all show analogous results.

## Appendix B: X-ray spectral analysis

All the objects in our sample have an estimate of the rest-frame 2-keV monochromatic flux derived from *XMM-Newton* photometric data. A detailed description of the procedure can be found in Section 4 of Lusso et al. (2020).

We have performed a full spectroscopic analysis for a subsample of 292 objects, which are all the objects in our sample at redshifts higher than 1.9, for which any discrepancy between the photometric and spectroscopic values can have major consequences in terms of cosmological applications. This comes as an extension of the X-ray spectroscopic analysis provided in Sacchi et al. (2022) for objects at redshifts higher than 2.5.

The goal of this analysis is to prove that not using fully spectroscopic X-ray fluxes does not introduce any bias in our results, while showing that part of the residual observed dispersion of the $L_X - L_{UV}$ relation can be attributed to the lower accuracy of photometric measurements at the same time. We followed the standard procedure from the *XMM-Newton* user manual to obtain the spectra. For each object, we extracted three spectra for the three *XMM-Newton* cameras (pn, MOS1, and MOS2). We then combined the two MOS spectra into a single one.

The fit procedure was performed with the package XSPEC version 12.12 (Arnaud 1996). We subtracted the background from the spectrum and then fitted it with a power-law model, considering Galactic photoelectric absorption. We fitted the pn and the MOS spectra simultaneously, imposing the same spectral shape and allowing for a varying normalisation constant between the two cameras. From the best fit, we estimated the monochromatic flux at 1 keV, the monochromatic flux at 2 keV, and the photon index Γ, together with their $1\sigma$ uncertainties. In Figure B.1 we show, as an example, the spectra and the best-fit model for three objects, with data of different quality and therefore different uncertainties on the determination of the monochromatic X-ray flux at 2 keV. In Figure B.2, we show the comparison between the monochromatic fluxes at 2 keV derived from this spectroscopic analysis with the ones obtain with the standard procedure. The relation between the two quantities was fitted with a linear relation, and the best fit is statistically consistent with a one-to-one relation, with the linear regression returning a slope of $m = 1.01 \pm 0.01$ as the best fit. In Figure B.3, we also show the histogram of the differences between the spectroscopic and the monochromatic 2 keV fluxes, expressed in units of the standard deviation $\sigma$. We also see from this distribution that there is no systematic shift between the two quantities. Neither is there a significant skewness of the distribution, the skewness parameter being $k = 0.27 \pm 0.30$.

From this comparison, we infer that by using the spectroscopic data only for a subsample of objects we are not introducing any systematics. At the same time, there is a significant scatter between the spectroscopic and the photometric flux estimates. We can assume that the spectroscopic analysis is the more accurate one. This means that for those objects for which we are (still) using photometric data, we are actually introducing a contribution to the total observed dispersion when fitting the $L_X - L_{UV}$ relation. We should also note that from the complete

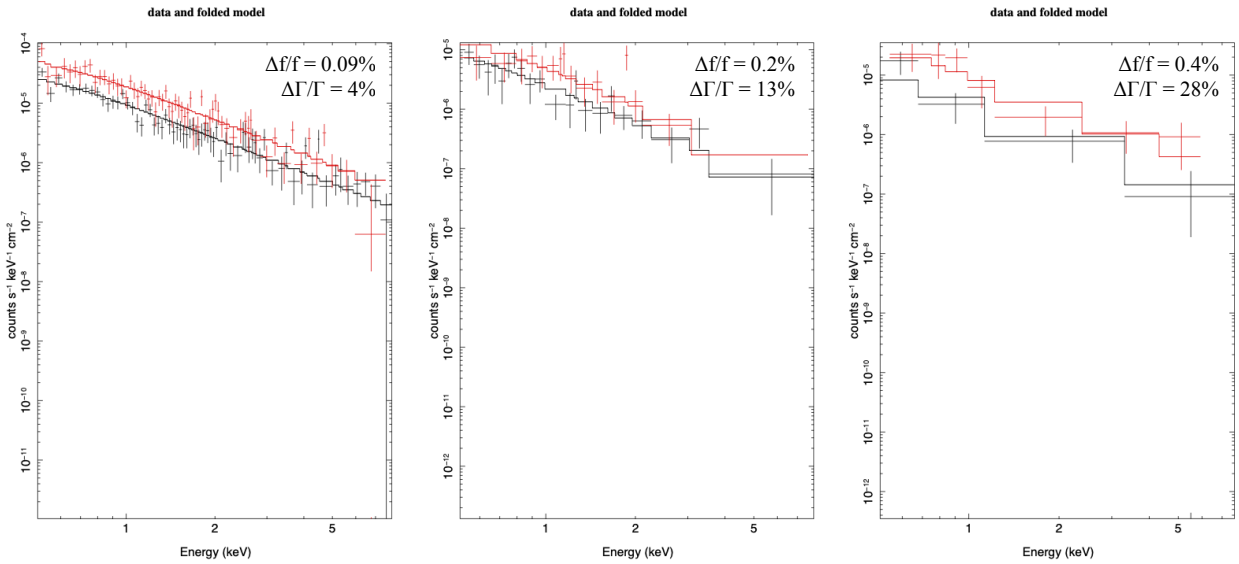


**Fig. B.1.** Example of X-ray spectrum and best fit of three sources at redshift 2.138, 2.144, 2.293. The pn spectrum is shown in red, and the MOS spectrum is shown in black. The relative uncertainties on the free parameters (the monochromatic flux at 2 keV and the photon index Γ) are shown as well.

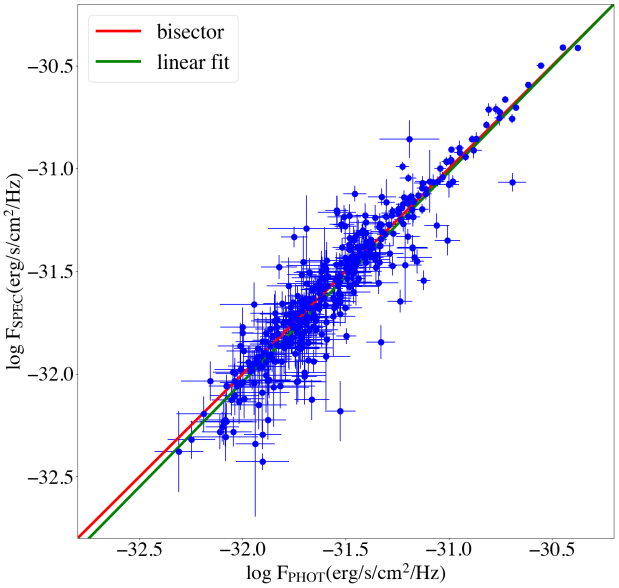


**Fig. B.2.** Comparison between photometrically derived 2-keV monochromatic fluxes and spectroscopically derived ones. The red line represents the one-to-one relation, while the green line is the best fit of the relation between the two quantities.

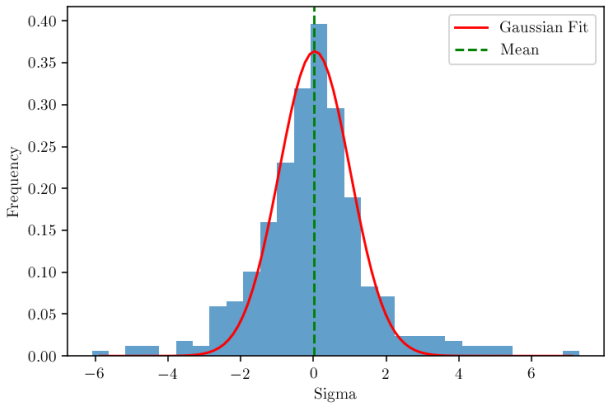


**Fig. B.3.** Histogram of differences between photometric and spectroscopic X-ray fluxes at 2 keV, shown in units of standard deviations. The red line shows the results of a Gaussian fit, which shows that the distribution is centred around zero. There is no significant skewness, as the skewness parameter turns out to be $k = 0.27 \pm 0.30$. This shows that there is no systematic shift between the two quantities.

X-ray spectroscopic analysis we are also able to check one by one that the observations are not affected by any bias, which is a possible cause of additional dispersion. A discussion of the contribution of X-ray observational issues to the total observed dispersion of the $L_X - L_{UV}$ relation will be addressed in a forthcoming paper. Analogous results in terms of the comparison between photometric and spectroscopic data are found when comparing the 1-keV monochromatic fluxes.